

Competing magnetic correlations and uniaxial anisotropy in $(\text{Fe}_{1-x}\text{Mn}_x)_2\text{AlB}_2$ single crystals

Taiki Shiotani ^{*}, Takeshi Waki , Yoshikazu Tabata, and Hiroyuki Nakamura 
Department of Materials Science and Engineering, Kyoto University, Kyoto 606-8501, Japan



(Received 7 March 2024; accepted 24 April 2024; published 15 May 2024)

We have succeeded for the first time in synthesizing single crystals of nanolaminated borides $(\text{Fe}_{1-x}\text{Mn}_x)_2\text{AlB}_2$ in the entire Fe–Mn composition range using the Al self-flux method, and have established $T-x$ and $H-T$ magnetic phase diagrams from the results of magnetization measurements. The ferromagnetic correlation of Fe_2AlB_2 is weakened with the Mn substitution, whereas the antiferromagnetic correlation of Mn_2AlB_2 is enhanced with the Fe up to $x = 0.65$. The spin direction in the magnetically ordered states changes from the a to the b axis with increasing Mn concentration and temperature. At $x = 0.31-0.46$, there are three magnetic phases; ferromagnetic, antiferromagnetic, and intermediate phases in between. At $x = 0.65$ and 0.74 , a spin-flop-like metamagnetic transition was observed at a finite field parallel to the spin direction. These observations indicate that in $(\text{Fe}_{1-x}\text{Mn}_x)_2\text{AlB}_2$ the ferromagnetic and antiferromagnetic correlations coexist and the uniaxial magnetic anisotropy competes between the a and b axes.

DOI: [10.1103/PhysRevMaterials.8.054412](https://doi.org/10.1103/PhysRevMaterials.8.054412)

I. INTRODUCTION

Transition-metal conductors with nanolaminated structure are of great interest as quasi-two-dimensional itinerant electron magnets in the viewpoints of both application and fundamental sciences. Since the discovery of the combination of metallic and ceramic properties, such as electrical and thermal conductivity, thermal and oxidative stability, and high hardness, in nanolaminated carbides and nitrides, called MAX phases [1], the design of magnetic properties has been intensively carried out to expand possible applications [2–5]. However, near-room-temperature magnetism has not been realized in the bulk materials. Recently, the nanolaminated transition-metal borides $M_2\text{AlB}_2$ ($M = \text{Cr}, \text{Mn}$ and Fe), which are members of a family called MAB phases, have attracted a lot of attention as the new candidates [6,7]. They form the orthorhombic structure in the space group $Cmmm$ (No. 65) with an alternating stacking of Al layer and $(\text{MB})_2$ slab along the b axis [Fig. 1(a)] [8,9]. The $(\text{MB})_2$ slab has strong covalent boron-zigzag chains and metallic $M-M$ bonding, which leads to the coexistence of metallic and ceramic properties [10]. In addition to the characters of environment-resistant conductors, they exhibit itinerant magnetism of $3d$ electrons in the $(\text{MB})_2$ slab; Cr_2AlB_2 is a Pauli paramagnet [11]. Mn_2AlB_2 shows antiferromagnetic ordering below the Néel temperature of $T_N = 313$ K with spins aligned along the b axis and the propagation vector of $\mathbf{q} = (0, 0, 1/2)$ [Fig. 1(b)] [12,13]. Fe_2AlB_2 is a ferromagnet with the Curie temperature of $T_C = 273$ K, an ordered moment of $1.2 \mu_B/\text{Fe}$, and the easy magnetization axis along the a axis [Fig. 1(c)] [14]. Density functional theory (DFT) calculations and angle-resolved photoemission spectroscopy revealed high density of states due to

nearly flat bands of $3d$ orbitals near the Fermi energy, which are associated with the magnetic ordering [15–17].

Since the discovery of its excellent magnetocaloric properties near room temperature [18], Fe_2AlB_2 has been extensively studied as a candidate for rare-earth-free and nontoxic magnetic refrigeration materials (for example, Refs. [14,16,19–26]). A detailed study using single crystal Fe_2AlB_2 revealed a substantial magnetocrystalline anisotropy with the anisotropy fields of 10 kOe along the b axis and 50 kOe along the c axis with respect to the easy a axis [14]. Subsequently, the magnetocaloric properties were reported to depend on the direction of the applied field, and then the significant contribution of the magnetocrystalline anisotropy was confirmed, providing a new guideline for maximizing the magnetocaloric potential of Fe_2AlB_2 [23,26]. Investigations on the solid solutions $(\text{Fe}, M)_2\text{AlB}_2$ ($M = \text{Ti}, \text{V}, \text{Mn}, \text{Co}$) and $\text{Fe}_2(\text{Al}, A)\text{B}_2$ ($A = \text{Si}, \text{Ga}, \text{Ge}$) have also been conducted to understand and control the magnetic properties [27–36]. In particular, $(\text{Fe}_{1-x}\text{Mn}_x)_2\text{AlB}_2$ is of interest because the magnetic correlation and uniaxial anisotropy are different between Fe_2AlB_2 and Mn_2AlB_2 . It is known that introducing antiferromagnetic correlation extends the temperature range of the magnetic transition [37]. Moreover, coexisting ferromagnetic and antiferromagnetic correlations and competing uniaxial magnetic anisotropy along the a and b axes can enrich the magnetic phase diagram and yield some specific events in magnetism, such as a metamagnetic transition, which can potentially broaden the application areas. However, there are some inconsistencies among the several previous reports on the magnetic properties of $(\text{Fe}_{1-x}\text{Mn}_x)_2\text{AlB}_2$. First, Chai *et al.* synthesized polycrystalline samples and performed magnetization measurements for $x \leq 0.8$. They found a gradually suppressed ferromagnetic correlation by the Mn substitution [29]. Subsequently, using magnetization and powder x-ray diffraction (XRD) measurements for $x \leq 0.25$ Du *et al.* proposed a re-entrant spin-glass transition below T_C at around

^{*}Corresponding author: shiotani.taiki.48e@st.kyoto-u.ac.jp

TABLE I. Initial compositions and actual compositions determined by WDX and ICP-MS. x corresponds to Mn/(Mn+Fe).

Initial composition	Nominal x	WDX		ICP-MS	
		Composition	x	Composition	x
Al ₅ Fe ₂ B _{1.33}	0	Fe ₂ Al _{1.00} B ₍₋₎	0	Fe ₂ Al _{1.05} B _{1.93}	0
Al ₅ Fe ₂ Mn _{0.1} B _{1.4}	0.05	(Fe _{0.87} Mn _{0.13}) ₂ Al _{0.96} B ₍₋₎	0.13	—	—
Al ₅ Fe ₂ Mn _{0.2} B _{1.47}	0.09	(Fe _{0.79} Mn _{0.21}) ₂ Al _{0.99} B ₍₋₎	0.21	(Fe _{0.79} Mn _{0.21}) ₂ Al _{1.04} B _{2.00}	0.21
Al ₅ Fe ₂ Mn _{0.4} B _{1.6}	0.17	(Fe _{0.69} Mn _{0.31}) ₂ Al _{0.98} B ₍₋₎	0.31	(Fe _{0.68} Mn _{0.32}) ₂ Al _{0.98} B _{2.00}	0.32
Al ₅ Fe _{1.68} Mn _{0.32} B _{1.6}	0.16	(Fe _{0.64} Mn _{0.36}) ₂ Al _{0.98} B ₍₋₎	0.36	(Fe _{0.64} Mn _{0.36}) ₂ Al _{1.09} B _{2.00}	0.36
Al _{2.08} Fe _{0.7} Mn _{0.3} B _{0.83}	0.3	(Fe _{0.54} Mn _{0.46}) ₂ Al _{0.93} B ₍₋₎	0.46	(Fe _{0.52} Mn _{0.48}) ₂ Al _{1.02} B _{1.99}	0.48
Al _{3.5} Fe _{0.7} Mn _{0.3} B	0.3	(Fe _{0.47} Mn _{0.53}) ₂ Al _{0.97} B ₍₋₎	0.53	(Fe _{0.44} Mn _{0.56}) ₂ Al _{1.01} B _{2.01}	0.56
Al _{3.5} Fe _{0.7} Mn _{0.3} B	0.3	(Fe _{0.36} Mn _{0.65}) ₂ Al _{0.95} B ₍₋₎	0.65	(Fe _{0.34} Mn _{0.66}) ₂ Al _{1.01} B _{2.06}	0.66
Al _{3.5} Fe _{0.5} Mn _{0.5} B	0.5	(Fe _{0.26} Mn _{0.74}) ₂ Al _{0.96} B ₍₋₎	0.74	—	—
Al ₁₀ Fe _{0.5} Mn _{0.5} B	0.5	(Fe _{0.13} Mn _{0.87}) ₂ Al _{0.98} B ₍₋₎	0.87	(Fe _{0.13} Mn _{0.87}) ₂ Al _{1.05} B _{1.99}	0.87
Al ₂₀ MnB	1	Mn ₂ Al _{0.99} B ₍₋₎	1	Mn ₂ Al _{1.06} B _{1.94}	1

$x = 0.25$ due to chemical disorder and competing ferromagnetic and antiferromagnetic interactions [31]. In addition, Cedervall *et al.* predicted a disordered ferrimagnetic state for $x = 0.5$ [30]. Recently, Potashnikov *et al.* synthesized polycrystalline samples for $x = 0-0.5, 0.75$ and 1, and performed magnetization and neutron powder diffraction (ND) measurements to obtain a $T-x$ magnetic phase diagram [32]. They observed an antiferromagnetic Bragg reflection for $x \geq 0.19$ and predicted a canted antiferromagnetic phase at intermediate Mn concentration. On the other hand, the corresponding anomaly was not observed in the magnetization measurements. The XRD and ND measurements also suggested that Mn atoms are homogeneously distributed in the sample, which is contrary to the previous reports [29–31]. The inconsistencies in the magnetism of $(\text{Fe}_{1-x}\text{Mn}_x)_2\text{AlB}_2$ arises from the difficulty in obtaining a single phase of the samples; these samples contain impurities such as $\text{Al}_{13}(\text{Fe}, \text{Mn})_4$, Al_2O_3 and $(\text{Fe}, \text{Mn})\text{B}$. Moreover, there is no report on the synthesis of $(\text{Fe}_{1-x}\text{Mn}_x)_2\text{AlB}_2$ single crystals except for $x = 0$ and 1. The single crystal growth can unravel a new magnetic phase as well as clarify the anisotropic magnetic properties, which could be helpful for improving the magnetocaloric property of Fe_2AlB_2 by tuning the magnetocrystalline anisotropy.

In this paper, we report the synthesis of $(\text{Fe}_{1-x}\text{Mn}_x)_2\text{AlB}_2$ single crystalline samples and discuss their magnetic properties based on magnetization measurements. We newly found a magnetic transition at intermediate Mn concentration, and then constructed detailed $T-x$ and $H-T$ magnetic phase diagrams.

II. EXPERIMENTS

A. Crystal growth

Single crystals of $(\text{Fe}_{1-x}\text{Mn}_x)_2\text{AlB}_2$ were grown by the Al self-flux method described in literature [12,14,38]. Al shots (Rare Metallic, 99.999%), Fe powder (Rare Metallic, 99.9%), crushed Mn flakes (Rare Metallic, 99.9%), and B chunks (Furuuchi Chemical, 99%) were used. Al shots and mixture of Fe, Mn, and B powders were placed in a boron nitride crucible and sealed in a quartz tube with a partial pressure of argon gas.

Table I shows the initial compositions of the raw materials and the nominal Mn concentrations x , which is the molar ratio of Mn/(Fe+Mn). In the case of nominally $0 \leq x \leq 0.3$, single crystals of $(\text{Fe}_{1-x}\text{Mn}_x)_2\text{AlB}_2$ were successfully grown by adopting an initial Al/(Fe+Mn) molar ratio of less than 3, which otherwise resulted in forming only $\text{Al}_{13}(\text{Fe}, \text{Mn})_4$ single crystals when nominally $x = 0-0.17$. The ampoule was initially heated up to 1200 °C over 2 h and held for 3 h, and then cooled down to 1180 °C over 1 h to avoid peritectic reactions, and slowly cooled down to 1080 °C over 30 h, at which the samples were centrifuged to separate single crystals from the flux. Platelike crystals similar to those of Fe_2AlB_2 [14] were obtained. The size was up to $5 \times 5 \times 0.2 \text{ mm}^3$ in the range of nominal $x = 0-0.17$ (actual $x = 0-0.36$), while up to $1 \times 1 \times 0.1 \text{ mm}^3$ for nominal $x = 0.3$ (actual $x = 0.46$) [Fig. 1(d)]. On the other hand, a large Al/(Mn+Fe) molar ratio was applicable for crystal growth with nominal $x \geq 0.3$. In this case, the tube was initially heated up to 1200 °C over 2 h, held for 3 h, and slowly cooled down to 800 °C–900 °C at a rate of 5 °C/h. Using a centrifuge, we separated strip-shaped crystals [Fig. 1(e)] similar to those of Mn_2AlB_2 [12]. The size was up to $3 \times 1 \times 0.1 \text{ mm}^3$ when $\text{Al}/(\text{Fe}+\text{Mn}) \leq 5$, while up to $10 \times 1 \times 0.2 \text{ mm}^3$ when $\text{Al}/(\text{Fe}+\text{Mn}) \geq 10$. Hexagonal platelike crystals of AlB_2 and prismatic crystals of $\text{Al}_{13}(\text{Fe}, \text{Mn})_4$ were also obtained from the melts with initial compositions of $\text{Al}_5\text{Fe}_{0.7}\text{Mn}_{0.3}\text{B}$ and $\text{Al}_5\text{Fe}_{0.5}\text{Mn}_{0.5}\text{B}$. Note that the actual Mn concentration of $(\text{Fe}_{1-x}\text{Mn}_x)_2\text{AlB}_2$ depends significantly on the Al/(Mn+Fe) ratio, as described below. The flux and impurity phases $\text{Al}_{13}(\text{Fe}, \text{Mn})_4$ and AlB_2 remaining on the surface were removed by dilute HCl aq immersion and concentrated KOH aq etching.

B. Crystal characterization and magnetic measurements

The grown crystals were characterized by powder x-ray diffraction (XRD) measurements with Cu $K_{\alpha 1}$ lines using X'Pert PRO Alpha-1 (PANalytical). The Rietveld refinement was performed using Rietan-FP [39]. Powder samples were prepared by crushing parts of the single crystals. The chemical composition of the grown crystals was analyzed by wavelength dispersive x-ray spectroscopy (WDX). We also measured the compositions of several batches by inductively coupled plasma mass spectrometry (ICP-MS) to estimate the

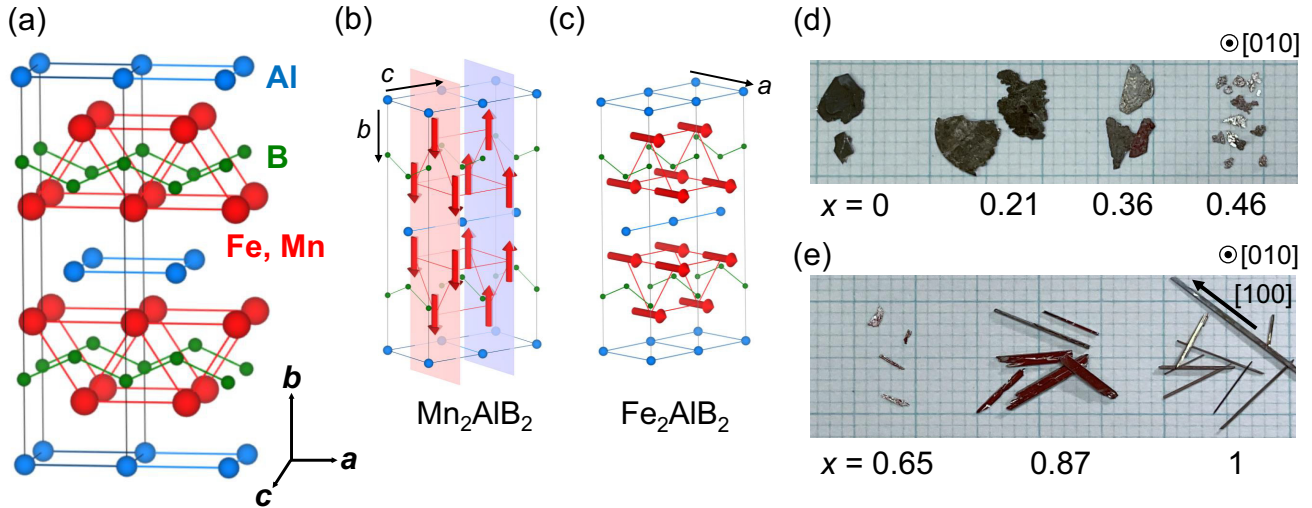


FIG. 1. (a) Crystal structure of $(\text{Fe}_{1-x}\text{Mn}_x)_2\text{AlB}_2$. [(b) and (c)] Magnetic structures of Mn_2AlB_2 and Fe_2AlB_2 , respectively, proposed in Refs. [12–14]. [(d) and (e)] Image of grown single crystals of $(\text{Fe}_{1-x}\text{Mn}_x)_2\text{AlB}_2$ with actual $x = 0$ –0.46 out of Al-self flux and those with $x = 0.65$ –1, respectively, on a millimeter scale. x is the actual Mn concentration measured by WDX.

content of boron, which was difficult to measure accurately by WDX. Crystal axes were identified using a Laue camera. Magnetization measurements were performed using a SQUID magnetometer (MPMS, Quantum Design) in the temperature range of 5–700 K and under magnetic fields up to 7 T. The magnetization above room temperature was measured using an oven option of the MPMS. For the temperature range of $T = 5$ –350 K, a piece of single crystal was used for magnetization measurement when $x = 0$ –0.46, while more than five crystals were used when $x = 0.65$ –1 with small crystal size and magnetization. For the high-temperature measurements using the oven option, we used several other single crystals in the same batch.

III. RESULTS

A. Sample characterization

Table I shows the chemical compositions of the grown crystals estimated by WDX. These were measured and averaged for more than three spots on the crystal surface and determined as averages for more than three crystals in the same batch. We have confirmed that the compositions of different batches prepared under the same conditions are practically identical. The listed compositions are normalized to $\text{Fe} + \text{Mn} = 2$ and the actual Mn concentration x is equal to $\text{Mn}/(\text{Mn} + \text{Fe})$. Table I shows that single crystals of $(\text{Fe}_{1-x}\text{Mn}_x)_2\text{AlB}_2$ have been successfully synthesized in the entire composition range. A slight deviation from the stoichiometry in Al is attributed to the mutual substitution of Fe and Al for the respective lattice sites, which has also been reported for Fe_2AlB_2 [20]. Actual x is higher than nominal x and depends on the initial $\text{Al}/(\text{Mn} + \text{Fe})$ molar ratio. For example, actual x obviously increased with initial $\text{Al}/(\text{Mn} + \text{Fe})$, despite the same nominal $x = 0.5$. We note that the standard deviations of x for all measured crystals were less than 0.05, suggesting no segregation into Fe-rich and Mn-rich aggregates in the crystal, consistent with the result

of the polycrystalline samples reported in Ref. [32] rather than Ref. [31].

As described in section II B, it was difficult to accurately determine the boron concentration by WDX. We performed ICP-MS and found that the compositions are in accordance with the ideal composition ratio of $(\text{Fe} + \text{Mn}) : \text{Al} : \text{B} = 2 : 1 : 2$ and the actual x values agree well with those estimated by WDX (see Table I). The overestimation of Al concentration may be due to residual flux at the surface. We will use the values measured by WDX as the Mn concentration in the following discussion.

Using the Laue method, the crystal orientation perpendicular to the flat surface was found to be [010] for all Mn concentrations. For the strip-shaped crystals, the longitudinal and transverse directions were identified as [100] and [001], respectively. These results are in agreement with previous reports of Fe_2AlB_2 and Mn_2AlB_2 [12,14].

Figure 2 shows the powder XRD profiles of $(\text{Fe}_{1-x}\text{Mn}_x)_2\text{AlB}_2$ with selected Mn concentrations at room temperature. We used powder samples prepared by crushing pieces of the single crystals. The reflections of the main phase for all Mn concentrations are indexed by the planes of an orthorhombic phase with the space group $Cmmm$. A small amount of Al and AlB_2 , residual flux and a by-product on the crystal surface, respectively, appeared in the XRD patterns of $x = 0.65$ and 0.74 due to insufficient etching.

The XRD patterns were refined by the Rietveld method using Rietan-FP [39]. The results of the fitting are shown in Fig. 2 and the refined parameters in Table S1 in Supplemental Material [40]. The unit-cell volumes of Fe_2AlB_2 and Mn_2AlB_2 are calculated to be 92.34 and 93.74 \AA^3 , respectively, which are close to the reported values of single crystals (92.23 [14] and 93.71 \AA^3 [12]). Figure 3 shows the refined lattice parameters and unit-cell volumes of $(\text{Fe}_{1-x}\text{Mn}_x)_2\text{AlB}_2$ as a function of Mn concentration x . Our results are in good agreement with but more detailed than the previous reports of polycrystalline samples [31,32]. These values do not

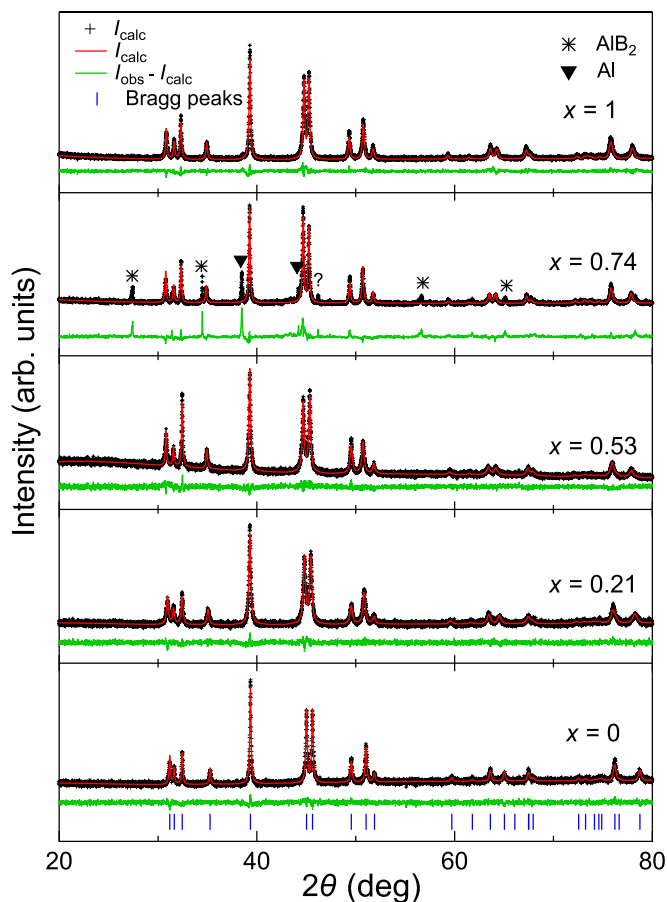


FIG. 2. Powder x-ray diffraction profiles of $(\text{Fe}_{1-x}\text{Mn}_x)_2\text{AlB}_2$ at room temperature. Results of the Rietveld refinement and expected Bragg reflections are also shown.

follow Vegard's law; the lattice parameters a and c start to decrease gradually at $x \simeq 0.5$ and 0.8 , respectively, whereas b has a broad hump at around $x = 0.25$, which was missing in the previous reports [31,32], and increases above $x \simeq 0.5$. The unit-cell volume shrinks above $x \simeq 0.8$ after expanding with increasing x . This nonlinear and nonmonotonic variation suggests that the spontaneous magnetovolume effect at room temperature depends sensitively on the Mn concentration x because the magnetic transition temperature varies at around room temperature, as shown in Fig. 10.

B. Magnetization

Figure 4 shows the temperature dependence of the magnetization for $x = 0$ – 0.46 . These samples show ferromagnetic behavior and the Curie temperature T_C decreases with increasing Mn concentration x . The Curie temperature of Fe_2AlB_2 ($x = 0$), which is $T_C = 275$ K, is close to literature data ($T_C = 273$ K [14]). There is neither cusp nor distinctive bifurcation between the data under zero-field cooled and field cooled condition at low temperature, suggesting the absence of the re-entrant spin-glass transition proposed in Ref. [31]. For $x = 0.31$ – 0.46 , a gradual ferromagnetic upturn was observed and dM/dT shows two-step anomalies at T_C and T_C^* . The transition temperatures depend on the direction of the

applied magnetic fields, except for $x = 0$ and 0.21 . Above T_C^* , another magnetic transition was observed for $x = 0.31$ – 0.46 ; for $x = 0.31$ and 0.36 , a bifurcation of the magnetization between the a axis and the b and c axes was observed below $T_N \simeq 300$ K and 320 K, respectively [insets of Figs. 4(d) and 4(e)], suggesting the presence of an antiferromagnetic ordering with spins aligned along the a axis. For $x = 0.46$, we can see in Fig. 4(f) a kink in the magnetization along the b axis around 360 K, also suggesting an antiferromagnetic ordering. Note that another kink was observed around $T = 620$ K, which is attributed to a ferromagnetic transition of impurities present in the sample; this anomaly was absent when a piece of crystal was used (see Fig. S1). The presence of an antiferromagnetic transition is also indicated by the inverse susceptibility, in which a hump anomaly was found above T_C^* for $x = 0.31$ – 0.46 (see Fig. S2).

The susceptibility in the paramagnetic region for $x = 0$ – 0.36 was fitted by the Curie-Weiss law $\chi = C/(T - \theta_{\text{CW}})$, where C is the Curie constant and θ_{CW} is the Curie-Weiss temperature. The estimated parameters are shown in Table II. The values of θ_{CW} are all positive, and at $x = 0.31$ and 0.36 they are close to T_C^* . The effective moment p_{eff} , estimated from C using the relation $C = \mu_B p_{\text{eff}}^2 / 3k_B$, does not vary significantly with x .

Figure 5 shows the field dependence of the magnetization for $x = 0$ – 0.46 at $T = 5$ K. The magnetic field along the b axis, perpendicular to the plane of the crystal, has been corrected to account for the demagnetizing field. The magnetization curves of these samples show typical ferromagnetic behavior. The saturation magnetization of $M_{\text{sat}} = 1.22 \mu_B / 3d$ -atom for Fe_2AlB_2 decreases with increasing x (see Table II). The easy magnetization axis of Fe_2AlB_2 is the a axis, and the hard axes are the b and c axes with anisotropy fields of $H_{\text{aniso}} \simeq 10$ and 50 kOe, respectively, which are in agreement with those reported in the previous report [14]. As Mn concentration x increases, the a axis becomes harder and the easy magnetization axis changes to the b axis at $x = 0.46$. The magnetic anisotropy also changes with temperature; for example, from the field dependence of the magnetization at 5 and 150 K (Fig. S3, see also Ref. [26] in Supplemental Material [40]), the easy magnetization axis changes from the a axis at 5 K to the b axis at 150 K without a spin-reorientation transition. Given the easy magnetization axis along the b axis at $T = 5$ K for $x = 0.46$, the upper temperature limit of the ferromagnetic phase with the a -easy axis is expected to decrease to 0 K with increasing x (see the FMA phase in Fig. 10). On the other hand, it is possible that the easy axis rotates in the a – b plane with temperature and Mn concentration. The evolution of the magnetic anisotropy at the intermediate x should be determined, for example, by the magnetic torque method. As shown in Fig. 6(a), the field-dependent magnetization exhibits a rapid increase at a finite magnetic field applied along the a axis for $x = 0.36$, which is parallel to the spin direction in the antiferromagnetic state. This is similarly observed for $x = 0.31$ and 0.46 (see Fig. S4). The corresponding peak in the dM/dH , appears below T_N and shifts to a lower field with decreasing temperature, splitting into doublets at H_{m_1} and H_{m_2} at low temperatures. With decreasing temperature further, H_{m_1} and H_{m_2} decrease and reach 0 Oe at T_C and T_C^* , respectively, and then the anomalies disappear

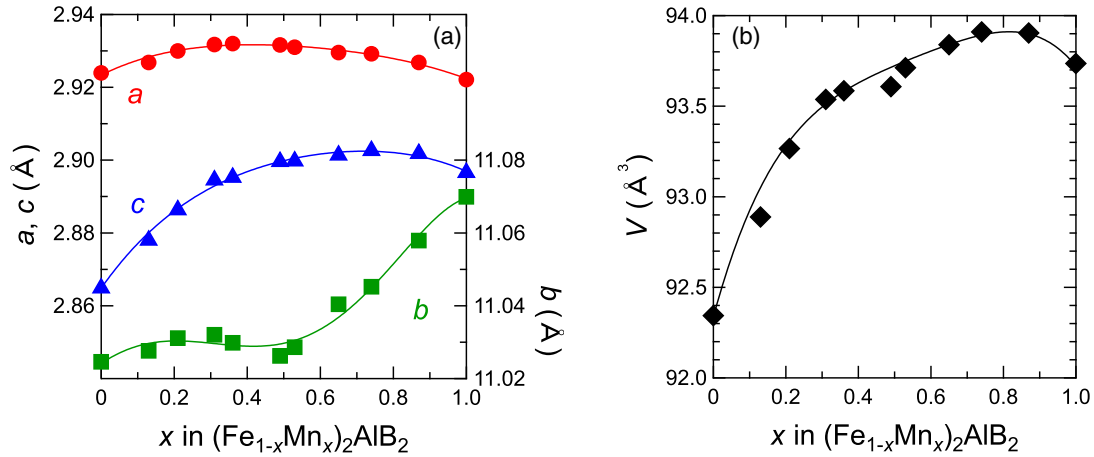


FIG. 3. Composition dependence of (a) lattice parameters and (b) unit-cell volume for $(\text{Fe}_{1-x}\text{Mn}_x)_2\text{AlB}_2$. The Mn concentration x was determined by WDX analysis.

at the lower temperature; for example, Fig. 6(b) shows that for $x = 0.36$, the peaks of dM/dH appear at H_{m_1} between 130 K ($>T_C = 110$ K) and 280 K ($<T_N = 320$ K), and those at H_{m_2} between 170 K ($>T_C^* = 150$ K) and 230 K. The peaks of dM/dH are broad and have no hysteresis (see Fig. S5). These observations suggest that the phase transition is of second order, although significant thermal fluctuations in the observed

temperature range may make it difficult to identify the nature of the transition. The magnetization above H_{m_1} gradually increases with a small slope, and is therefore considered to be in the induced ferromagnetic state: the trend is clearly seen in the Arrott plot (Fig. S6). This suggests that at $H_{m_2} < H < H_{m_1}$ the magnetic structure has an antiferromagnetic component and the spins are rotated towards the

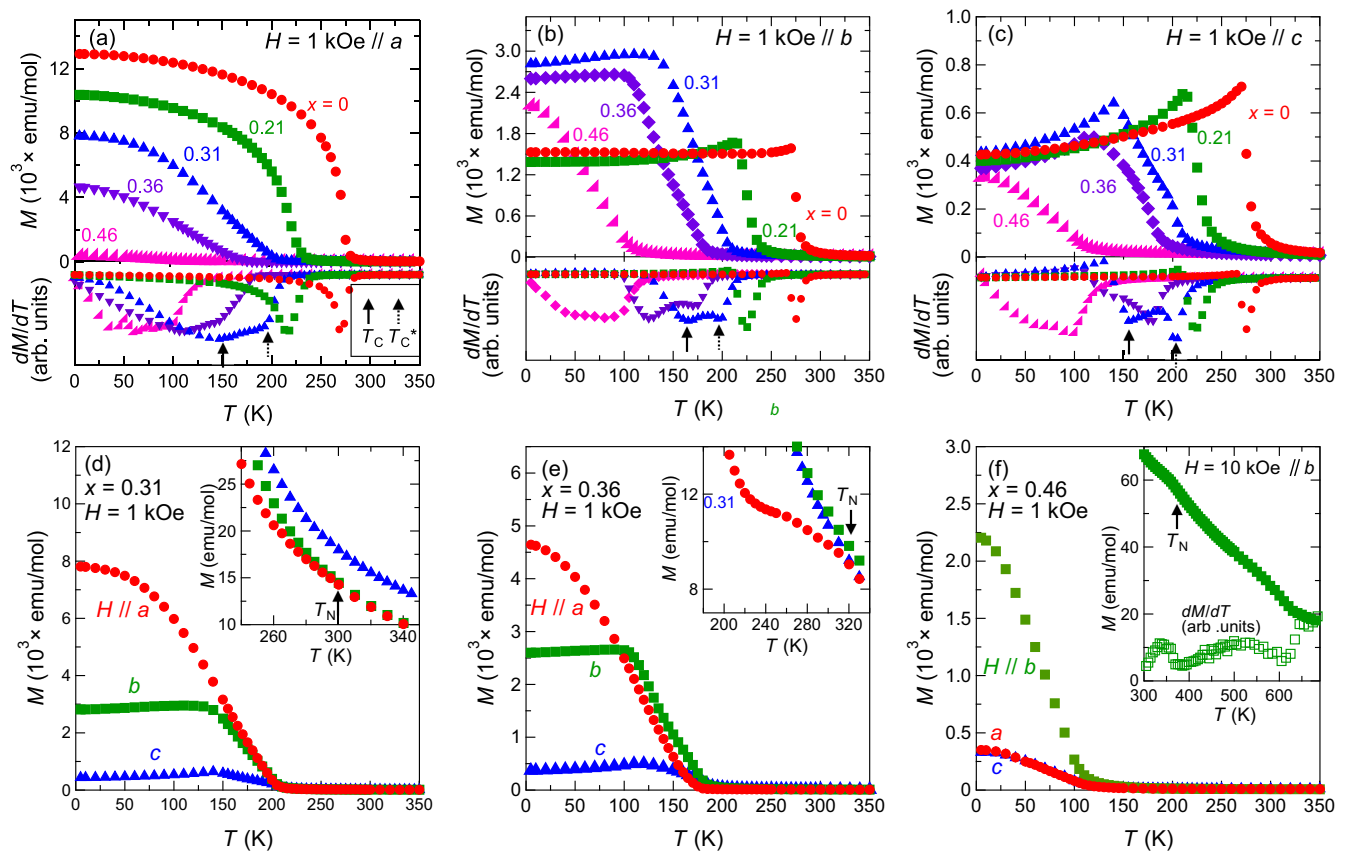


FIG. 4. [(a)–(c)] Temperature dependence of the magnetization and its derivative dM/dT for $x = 0$ – 0.46 under a magnetic field of $H = 1$ kOe along the a , b , and c axes. The solid and dashed arrows indicate T_C and T_C^* , respectively. [(d)–(f)] Temperature dependence of the magnetization along the three crystallographic axes for $x = 0.31$, 0.36 , and 0.46 . The insets show the data in high-temperature regions.

TABLE II. Transition temperatures (T_C , T_C^* , T_N) and the results of Curie-Weiss fitting (p_{eff} , θ_{CW}) for $(\text{Fe}_{1-x}\text{Mn}_x)_2\text{AlB}_2$. T_C , T_C^* , p_{eff} , and θ_{CW} were estimated from the magnetization along the a axis.

x (K)	T_C (K)	T_C^* (K)	T_N (K)	p_{eff} ($\mu_B/3d$ -atom)	θ_{CW} (K)	M_{sat} ($\mu_B/3d$ -atom)
0	275(5)	–	–	2.28	280	1.22
0.21	220(5)	–	–	2.15	240	0.93
0.31	150(10)	205(10)	300(20)	2.33	205	0.71
0.36	110(10)	150(10)	320(10)	2.26	177	0.57
0.46	40(20)	95(20)	350(15)	–	–	0.23
0.65	–	–	385(5)	–	–	–
0.74	–	–	350(10)	–	–	–
0.87	–	–	340(5)	–	–	–
1	–	–	315(5)	–	–	–

ferromagnetic state with increasing field. This should be confirmed by neutron diffraction experiments.

Figure 7 shows the temperature dependence of the susceptibility measured at 10 kOe for $x = 0.65$ –1. Mn_2AlB_2 , which is already known to be an antiferromagnet, shows the same behavior as in the previous report [12]. The Néel temperature of Mn_2AlB_2 is $T_N = 315$ K, and below T_N the magnetization decreases significantly only along the b axis, which is the spin direction. Similar anisotropic behavior was observed for $x = 0.65$ –0.87, showing that they are similar antiferromagnets. T_N increases with decreasing Mn concentration x (Table II), suggesting that the antiferromagnetic correlation is enhanced by the Fe substitution. When x decreases to 0.65, the spin direction changes from the b axis to the a axis, which is comparable to the estimated spin direction in the antiferromagnetic phase at low Mn concentrations ($x = 0.31$ and 0.36). A slight upturn at low temperature was observed for $x = 0.87$ and 1, suggesting the presence of a small amount of paramagnetic impurities. On the other hand, for $x = 0.65$ and 0.74, a Curie-type temperature dependence was observed along particular directions, namely, the b and c axes for $x = 0.65$ and the c axis for $x = 0.74$. This is ascribed to the enhanced ferromagnetic or antiferromagnetic correlation due to the Fe substitution.

Figure 8 shows the field dependence of the magnetization for $x = 0.65$ –0.87 at $T = 5$ K. While the magnetization increases linearly along all the axes for $x = 0.87$ and 1 (Fig. S7), a metamagnetic-like transition was observed along the a axis for $x = 0.65$ and along the b axis for $x = 0.74$. Figure 9 shows the field-dependent magnetization and its derivative dM/dH

measured at different temperatures for $x = 0.65$ and 0.74. The metamagnetic-like transition was observed at the field parallel to the spin direction in the whole measured temperature range of $T = 5$ –350 K, and probably up to T_N . Above the transition field H_m , the magnetization is not saturated but increases linearly, which is characteristic of the spin-flop process. In general, a metamagnetic transition occurs with field hysteresis and a first-order discontinuous increase in magnetization. On the other hand, at the transition, the magnetization increases rapidly but continuously, and dM/dH shows a broad peak even at $T = 5$ K. Therefore this metamagnetic-like transition is considered to be of the gradual spin-flop type, which occurs in the case of weak magnetocrystalline anisotropy [41–45]. Note that there may be small misalignment of the crystals in the sample, which can lead to a broadening of the transition from a first to a second order type [42]. In a uniaxial antiferromagnet, the metamagnetic field can be simply written as $H_m = \sqrt{2H_A H_E - H_A^2}$, where H_A and H_E are the magnitudes of the anisotropy field and the antiferromagnetic exchange field, respectively. Given the near-room-temperature antiferromagnetic ordering, the exchange field H_E is likely to be large and thus the anisotropy field H_A should be small in order to induce the transition at the relatively low fields (Fig. 9). This conjecture agrees with the condition of the gradual spin-flop transition, and one of the proposed scenarios for the small H_A is a competition of the uniaxial magnetic anisotropy of the a and b axes. Moreover, H_m takes a maximum at an intermediate temperature below T_N . This may be ascribed to a competition between the magnetic anisotropy and the antiferromagnetic correlation.

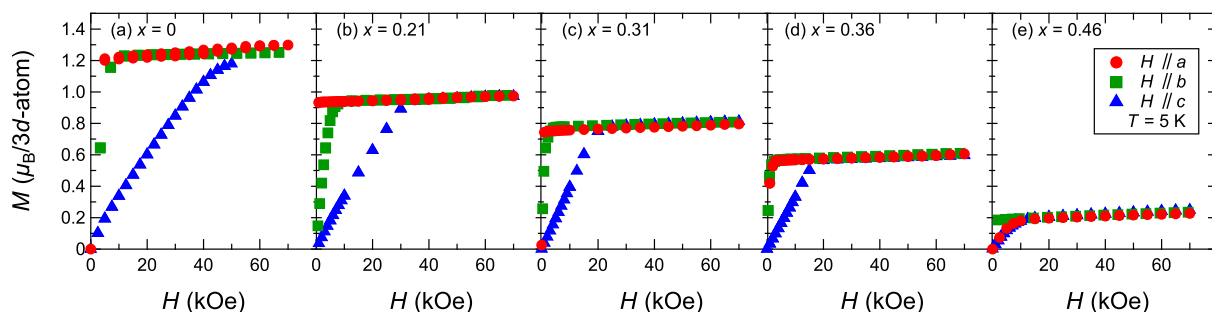


FIG. 5. Field dependence of the magnetization for $x = 0$ –0.46 at $T = 5$ K.

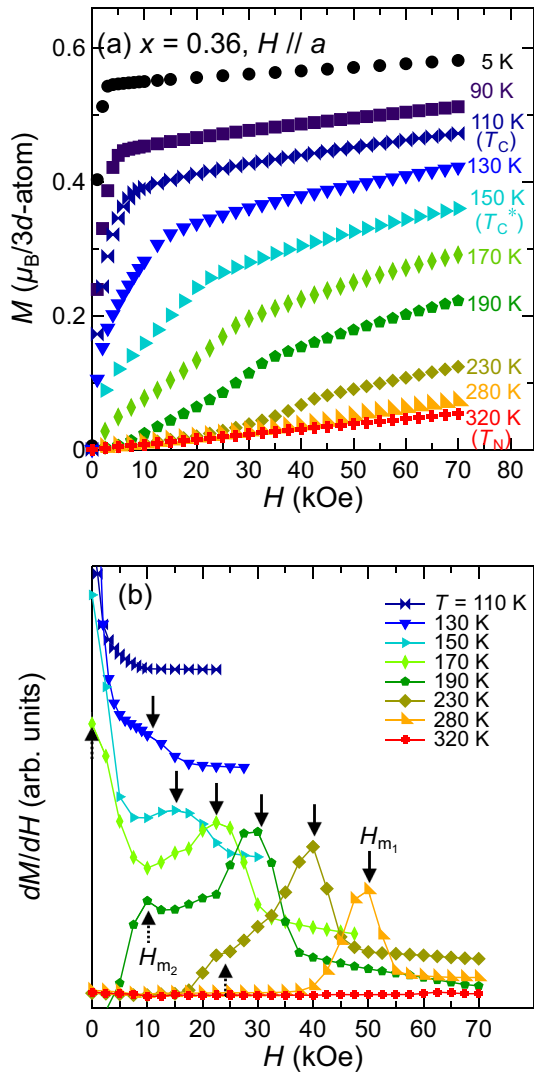


FIG. 6. (a) Magnetization curves and (b) their field derivatives at different temperatures parallel to the a axis for $x = 0.36$.

IV. MAGNETIC PHASE DIAGRAMS

Based on the results of magnetization measurements, we tried to construct magnetic phase diagrams of $(\text{Fe}_{1-x}\text{Mn}_x)_2\text{AlB}_2$. Figure 10 shows the $T-x$ magnetic phase diagram. It consists of three distinct magnetic phases; ferromagnetic (FM) phases and antiferromagnetic (AFM) phases, and an intermediate (FM2) phase. In the FM phase, the easy magnetization axis changes with temperature and Mn concentration; FM with the a -easy-magnetization axis (FMa) is in the low x region, while FM with b -easy-magnetization axis (FMb) is close to the FM2 phase. In the AFM phase, the spin direction changes from the b axis (AFMb) to the a axis (AFMa) below $x \sim 0.7$. The propagation vector is expected to be $\mathbf{q} = (0, 0, 1/2)$ as given by the previous neutron powder diffraction measurements [13,32]. Although Potashnikov *et al.* [32] reported an antiferromagnetic transition below T_C at $x = 0.19$ and 0.23 (see open markers in Fig. 10), our magnetization data show no corresponding anomaly for $x < 0.21$. Note that the powder sample used for the neutron

diffraction measurements contained impurity phases, which may lead to extrinsic magnetic diffraction. Otherwise, the observed transition temperatures are approximately close to the literature data [32].

The Néel temperature T_N has a maximum at around $x = 0.6$ and drops rapidly below $x = 0.6$, while the Curie temperature T_C decreases monotonically with increasing x . The Curie temperature was found to split into two transitions at T_C and T_C^* at around $x = 0.2$, leading to the intermediate FM2 phase. The FM2 phase is surrounded by the FMb and AFMa phases. In this region, a rapid increase of magnetization was observed under the finite field along the a axis (Fig. 6). Therefore the FM2 phase is considered to have both a ferromagnetic component along the b axis and a small antiferromagnetic component along the a axis. The magnetic state is comparable to the canted antiferromagnetic structure with $\mathbf{q} = (0, 0, 1/2)$ predicted by neutron powder diffraction experiments [32]. Neutron diffraction measurements on single crystals are future work. These complex variations of the spin direction at the intermediate Mn concentration seem to be difficult to be explained by the rigid-band model. Lu *et al.* suggested that the $3d$ orbitals, which contribute to the high density of states $D(E)$ and the nearly flat bands near the Fermi level E_F , are different between Fe_2AlB_2 (d_{xy}) and Mn_2AlB_2 (e_g), and give rise to the different spin directions [17]. Thus, it is possible that the intermediate nature of the $3d$ -band structure near E_F makes the uniaxial magnetic anisotropy competitive in $(\text{Fe}_{1-x}\text{Mn}_x)_2\text{AlB}_2$. In Fig. 10, there appears to be a quadruple critical point around $(x, T) = (0.2, 200 \text{ K})$. However, systematic studies using samples with more finely controlled compositions are needed to elucidate its nature.

From the temperature evolution of the anomalies observed in the magnetic isotherm measured under the field along the a axis for $x = 0.36$, we constructed a $H-T$ magnetic phase diagram [Fig. 11(a)]. We obtained those of similar shape for $x = 0.31$ and 0.46 (Fig. S8). The AFMa phase is located in the high-temperature region and expands as Mn concentration increases. It undergoes two-step transitions to a field-induced ferromagnetic phase with increasing field. Given that the transition field H_{m1} and H_{m2} decrease to zero at around T_C and T_C^* , respectively, the intermediate phase in Fig. 11(a) is considered to be identical to the FM2 phase in the $T-x$ diagram (Fig. 10).

Figure 11(b) shows the $H-T$ magnetic phase diagram under the field applied along the a axis for $x = 0.65$. The one under the field applied along the b axis for $x = 0.74$ is shown in Fig. S9. The spin-flop (SF) phases are located above the dome-shaped AFM phase below T_N . The transition between the SF and the AFM phases is gradual and continuous. This is ascribed to the weak uniaxial magnetic anisotropy competing between along the a and b axes. This may lead to the spin rotation in the a - b plane. A field-induced ferromagnetic state was not reached in the field range of 0–70 kOe. A higher field is necessary to know whether the SF state undergoes another antiferromagnetic phase transition or saturates to a ferromagnetic state.

Finally, we show the schematic three-dimensional $H-T-x$ magnetic phase diagram at the field along the a axis (Fig. 12). In the low- x region, the AFM phase is

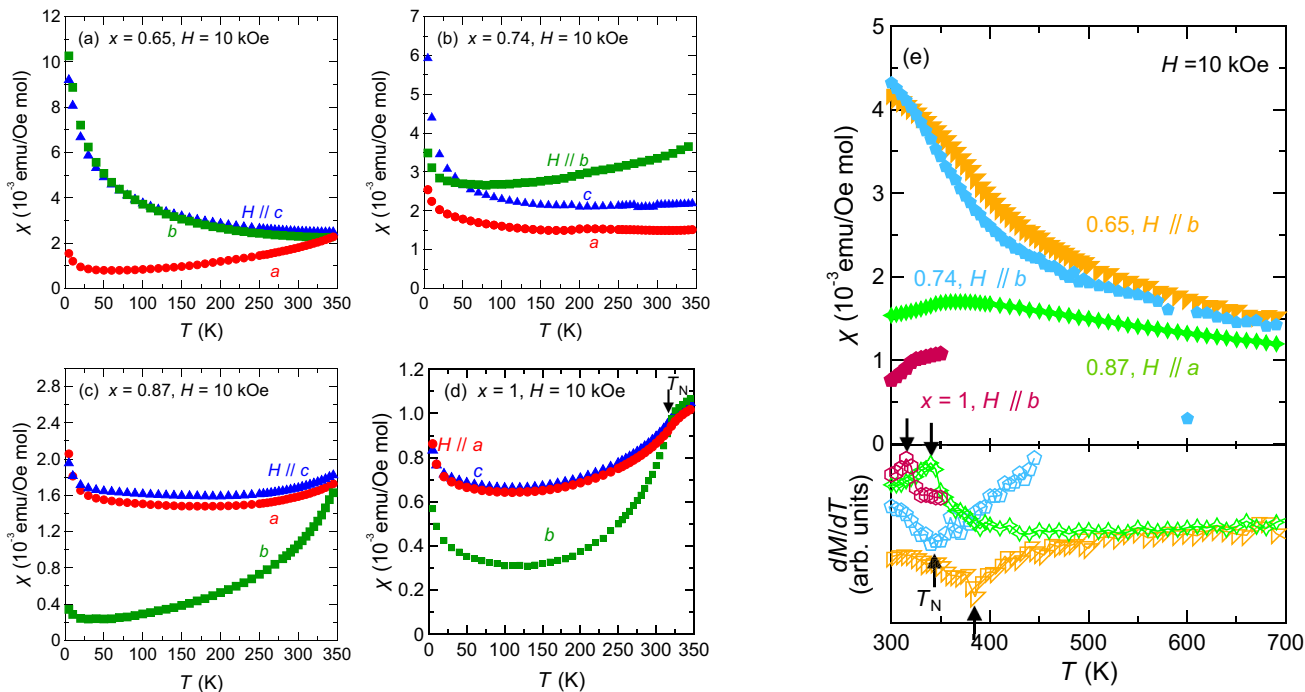


FIG. 7. [(a)–(d)] Temperature dependence of the susceptibility for $x = 0.65$ – 1 . (e) The susceptibility for $x = 0.65$ – 0.87 above 300 K measured using the oven option.

robust to magnetic fields in the high temperature region because it is far from the FM phase. With increasing x , the critical field H_{m_2} near T_N becomes higher, and the transition temperature T_C^* , where H_{m_2} reaches 0 Oe, decreases due to the suppressed ferromagnetic and enhanced antiferromagnetic correlations. Between the AFM and FM phases, there is an intermediate phase FM2, and its region extends similarly with increasing x . Above $x \simeq 0.6$, where the ferromagnetic correlation disappears, only the AFM phase is present below T_N at low fields, and it rapidly becomes robust to magnetic fields even for the low temperature region. Under fields higher than H_m , a spin-flop phase SF appears. Given that it arises with a dominant antiferromagnetic component as a result of a competition of uniaxial magnetic anisotropy, its character is different from the FM2 phase with a dominant ferromagnetic component, which arises from a competition between ferromagnetic and antiferromagnetic correlations. Although the details are unclear at present, it is expected that

the SF phase will lie below the FM2 phase (i.e., $H_m < H_{m_2}$) or appear as a drastic change in the character of the FM2 phase (i.e., H_{m_2} is identical to H_m) at $x \simeq 0.6$.

V. CONCLUSION

Single crystals of nanolaminated borides ($\text{Fe}_{1-x}\text{Mn}_x$) $_2\text{AlB}_2$ were synthesized in the entire Fe–Mn composition range using the self-flux method, and structural and magnetization measurements were performed. The Curie temperature of $T_C \simeq 275$ K and the spontaneous moment of $M_{\text{sat}} \simeq 1.2 \mu_B/\text{Fe}$ in Fe_2AlB_2 decrease monotonically with increasing Mn concentration, whereas the Néel temperature has a maximum of $T_N \simeq 385$ K at $x = 0.65$. The spin direction in the ferromagnetic and antiferromagnetic states at 5 K changes from the a axis to the b axis as the Mn concentration increases to $x \simeq 0.4$ and 0.7 , respectively. In the range of $x = 0.31$ – 0.46 , we observed an antiferromagnetic ordering

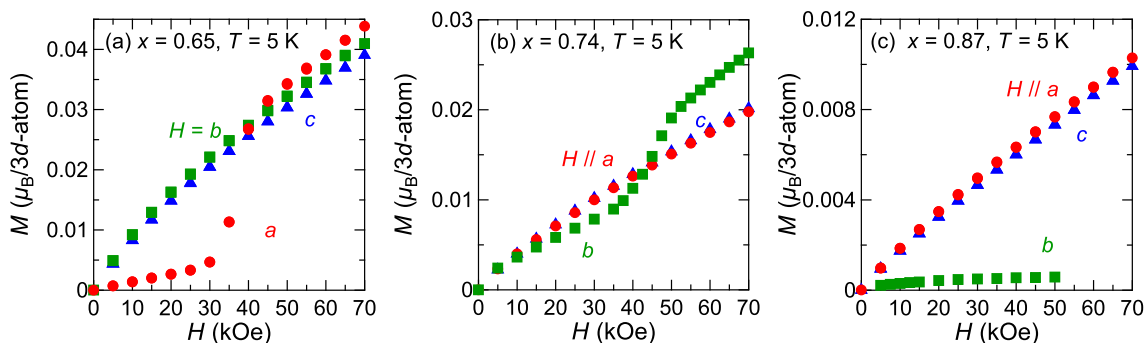


FIG. 8. Magnetization curves for $x = 0.65$ – 0.87 at 5 K.

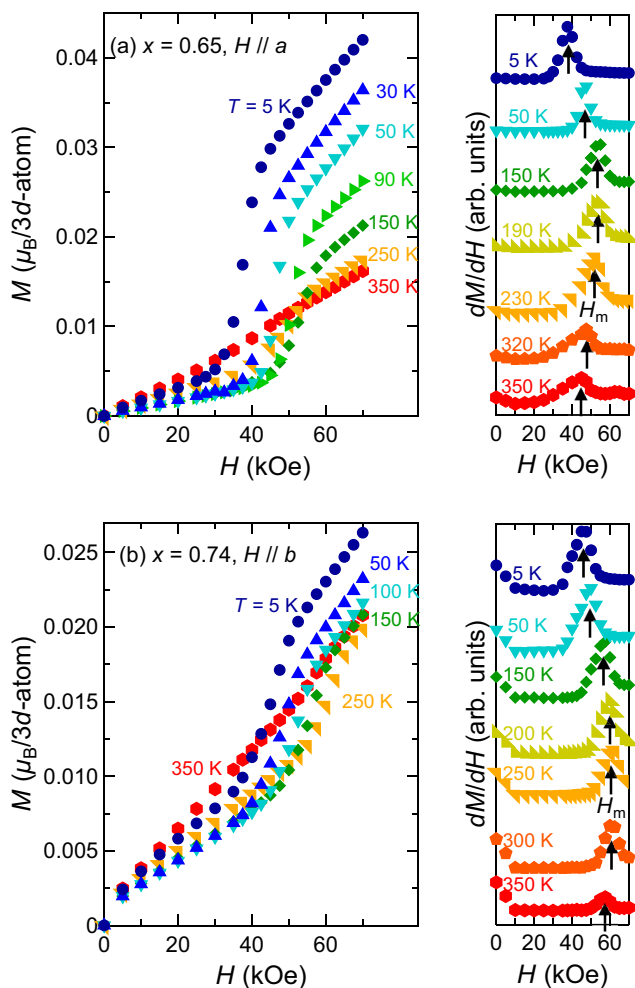


FIG. 9. Magnetization curves and their field derivatives at different temperatures (a) parallel to the a axis for $x = 0.65$ and (b) parallel to the b axis for $x = 0.74$.

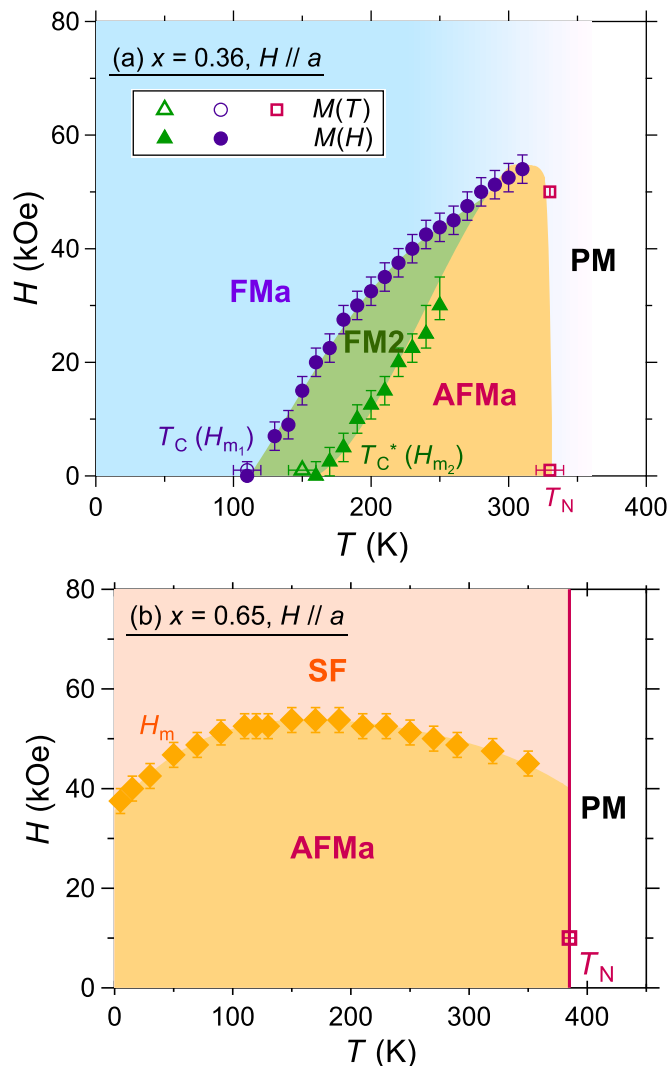


FIG. 11. H - T magnetic phase diagrams for (a) $x = 0.31$ and (b) $x = 0.65$ under the field applied to the a axis. Closed and open marks represent the data obtained from the field-dependent and temperature-dependent magnetization, respectively.

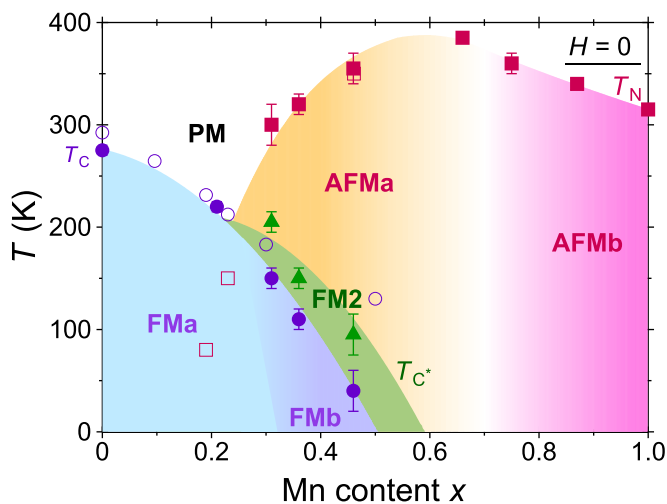


FIG. 10. T - x magnetic phase diagram at zero field for $(\text{Fe}_{1-x}\text{Mn}_x)_2\text{AlB}_2$. Open markers represent transition temperatures estimated from neutron powder diffraction experiments [32].

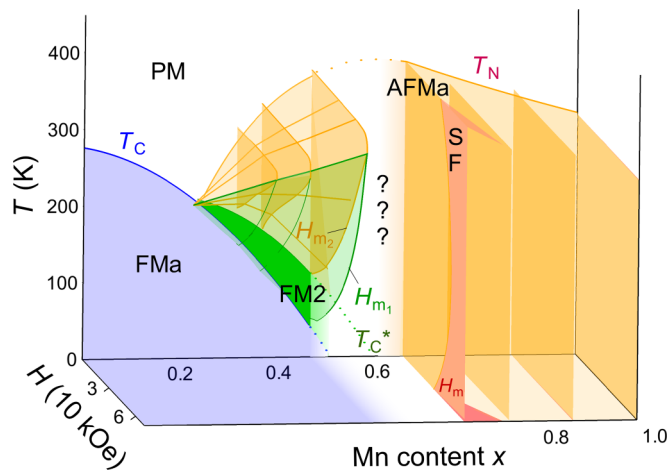


FIG. 12. Schematic three-dimensional magnetic phase diagram of $(\text{Fe}_{1-x}\text{Mn}_x)_2\text{AlB}_2$ when the magnetic field is applied along the a axis, for reader's convenience.

above T_C^* and two-step ferromagnetic transitions at T_C and T_C^* along the a axis. In this intermediate phase FM2, both the ferromagnetic correlations of the b -axis spin component and the antiferromagnetic correlations of the a -axis spin component coexist. At $x = 0.65$ and 0.74 , a gradual spin-flop transition was observed below T_N in the field along the a and b axes, respectively, due to the weak uniaxial magnetic anisotropy caused by the competition between the a and b axes. Thus the magnetic properties of $(\text{Fe}_{1-x}\text{Mn}_x)_2\text{AlB}_2$ are found to be sensitive to the composition, temperature and field. Our findings could further expand the variety of

potential applications as an environment-resistant itinerant magnet.

ACKNOWLEDGMENTS

The authors thank Y. Uno for their help with composition analysis. This work was supported by SPRING, Support for Pioneering Research Initiated by the Next Generation of Kyoto University, and JSPS KAKENHI Grant No. JP24KJ1325..

-
- [1] M. W. Barsoum, *Prog. Solid State Chem.* **28**, 201 (2000).
- [2] Z. Liu, T. Waki, Y. Tabata, K. Yuge, H. Nakamura, and I. Watanabe, *Phys. Rev. B* **88**, 134401 (2013).
- [3] Z. Liu, T. Waki, Y. Tabata, and H. Nakamura, *Phys. Rev. B* **89**, 054435 (2014).
- [4] A. Mockute, M. Dahlqvist, J. Emmerlich, L. Hultman, J. M. Schneider, P. O. A. Persson, and J. Rosen, *Phys. Rev. B* **87**, 094113 (2013).
- [5] S. Lin, P. Tong, B. S. Wang, Y. N. Huang, W. J. Lu, D. F. Shao, B. C. Zhao, W. H. Song, and Y. P. Sun, *J. Appl. Phys.* **113**, 053502 (2013).
- [6] S. Kota, M. Sokol, and M. W. Barsoum, *Int. Mater. Rev.* **65**, 226 (2020).
- [7] A. Rosenkranz, D. Zambrano, A. Przyborowski, R. Shah, and A. M. Jastrzębska, *Adv. Mater. Interfaces* **9**, 2200869 (2022).
- [8] W. Jeitschko, *Acta Crystallogr. Sect. B* **25**, 163 (1969).
- [9] Y. B. Kuz'ma and N. F. Chaban, *Izv. Akad. Nauk SSSR, Neorg. Mater.* **5**, 384 (1969).
- [10] Y. Zhou, H. Xiang, F.-Z. Dai, and Z. Feng, *Mater. Res. Lett.* **5**, 440 (2017).
- [11] S. Kota, W. Wang, J. Lu, V. Natu, C. Opagiste, G. Ying, L. Hultman, S. J. May, and M. W. Barsoum, *J. Alloys Compd.* **767**, 474 (2018).
- [12] T. N. Lamichhane, K. Rana, Q. Lin, S. L. Bud'ko, Y. Furukawa, and P. C. Canfield, *Phys. Rev. Mater.* **3**, 064415 (2019).
- [13] D. Potashnikov, E. Caspi, A. Pesach, A. Hoser, S. Kota, L. Verger, M. Barsoum, I. Felner, A. Keren, and O. Rivin, *J. Magn. Mater.* **471**, 468 (2019).
- [14] T. N. Lamichhane, L. Xiang, Q. Lin, T. Pandey, D. S. Parker, T.-H. Kim, L. Zhou, M. J. Kramer, S. L. Bud'ko, and P. C. Canfield, *Phys. Rev. Mater.* **2**, 084408 (2018).
- [15] L. Ke, B. N. Harmon, and M. J. Kramer, *Phys. Rev. B* **95**, 104427 (2017).
- [16] Z. Liu, S. Yang, H. Su, L. Zhou, X. Lu, Z. Liu, J. Gao, Y. Huang, D. Shen, Y. Guo, H. Weng, and S. Wang, *Phys. Rev. B* **101**, 245129 (2020).
- [17] X. Lu, H. Su, L. Zhou, J. Gao, M. Li, J. Yuan, Z. Liu, Y. Huang, S. Wang, H. Weng, Y. Guo, Z. Liu, and D. Shen, *Phys. Rev. B* **103**, 195144 (2021).
- [18] X. Tan, P. Chai, C. M. Thompson, and M. Shatruk, *J. Am. Chem. Soc.* **135**, 9553 (2013).
- [19] S. Sharma, A. E. Kovalev, D. J. Rebar, D. Mann, V. Yannello, M. Shatruk, A. V. Suslov, J. H. Smith, and T. Siegrist, *Phys. Rev. Mater.* **5**, 064409 (2021).
- [20] B. T. Lejeune, D. L. Schlageel, B. A. Jensen, T. A. Lograsso, M. J. Kramer, and L. H. Lewis, *Phys. Rev. Mater.* **3**, 094411 (2019).
- [21] D. K. Mann, Y. Wang, J. D. Marks, G. F. Strouse, and M. Shatruk, *Inorg. Chem.* **59**, 12625 (2020).
- [22] Y. M. Oey, J. D. Bocarsly, D. Mann, E. E. Levin, M. Shatruk, and R. Seshadri, *Appl. Phys. Lett.* **116**, 212403 (2020).
- [23] R. Barua, B. Lejeune, L. Ke, G. Hadjipanayis, E. Levin, R. McCallum, M. Kramer, and L. Lewis, *J. Alloys Compd.* **745**, 505 (2018).
- [24] K. Han, M. Li, M. Gao, X. Wang, J. Huo, and J.-Q. Wang, *J. Alloys Compd.* **908**, 164663 (2022).
- [25] B. Lejeune, R. Barua, Y. Mudryk, M. Kramer, R. McCallum, V. Pecharsky, and L. Lewis, *J. Alloys Compd.* **886**, 161150 (2021).
- [26] H. B. Tran, H. Momida, Y.-i. Matsushita, K. Sato, Y. Makino, K. Shirai, and T. Oguchi, *Phys. Rev. B* **105**, 134402 (2022).
- [27] S. Wang, P. Liu, J. Chen, and W. Cui, *AIP Adv.* **12**, 035235 (2022).
- [28] S. Hirt, F. Yuan, Y. Mozharivskyj, and H. Hillebrecht, *Inorg. Chem.* **55**, 9677 (2016).
- [29] P. Chai, S. A. Stoian, X. Tan, P. A. Dube, and M. Shatruk, *J. Solid State Chem.* **224**, 52 (2015).
- [30] J. Cedervall, M. S. Andersson, D. Iuşan, E. K. Delczeg-Czirjak, U. Jansson, P. Nordblad, and M. Sahlberg, *J. Magn. Mater.* **482**, 54 (2019).
- [31] Q. Du, G. Chen, W. Yang, J. Wei, M. Hua, H. Du, C. Wang, S. Liu, J. Han, Y. Zhang, and J. Yang, *J. Phys. D: Appl. Phys.* **48**, 335001 (2015).
- [32] D. Potashnikov, E. N. Caspi, A. Pesach, S. Kota, M. Sokol, L. A. Hanner, M. W. Barsoum, H. A. Evans, A. Eyal, A. Keren, and O. Rivin, *Phys. Rev. Mater.* **4**, 084404 (2020).
- [33] R. Barua, B. Lejeune, B. Jensen, L. Ke, R. McCallum, M. Kramer, and L. Lewis, *J. Alloys Compd.* **777**, 1030 (2019).
- [34] Z. Zhang, G. Yao, L. Zhang, P. Jia, X. Fu, W. Cui, and Q. Wang, *J. Magn. Mater.* **484**, 154 (2019).
- [35] M. S. Hossain, K. Stillwell, S. Agbo, A. Pathak, and M. Khan, *J. Magn. Mater.* **571**, 170576 (2023).
- [36] B. Beckmann, T. A. El-Melegy, D. Koch, U. Wiedwald, M. Farle, F. Maccari, J. Snyder, K. P. Skokov, M. W. Barsoum, and O. Gutfleisch, *J. Appl. Phys.* **133**, 173903 (2023).
- [37] N. de Oliveira and P. von Ranke, *Phys. Rep.* **489**, 89 (2010).

- [38] M. Ade and H. Hillebrecht, *Inorg. Chem.* **54**, 6122 (2015).
- [39] K. M. F. Izumi, *Solid State Phenom.* **130**, 15 (2007).
- [40] See Supplemental Material at <http://link.aps.org/supplemental/10.1103/PhysRevMaterials.8.054412> for the additional results of the experiments.
- [41] N. Ashcroft and N. Mermin, *Solid State Physics* (Harcourt College, San diego, 1976)
- [42] H.-F. Li, *npj Comput. Mater.* **2**, 16032 (2016).
- [43] J. Casey, S. S. Samatham, C. Burgio, N. Kramer, A. Sawon, J. Huff, and A. K. Pathak, *Phys. Rev. Mater.* **7**, 074402 (2023).
- [44] E. Emmanouilidou, J. Liu, D. Graf, H. Cao, and N. Ni, *J. Magn. Magn. Mater.* **469**, 570 (2019).
- [45] S. S. Samatham, S. Barua, and K. Suresh, *J. Magn. Magn. Mater.* **444**, 439 (2017).